

Direct numerical simulations of the κ -mechanism

I. Radial modes in the purely radiative case

T. Gastine and B. Dintrans

Observatoire Midi-Pyrénées, UMR5572, CNRS et Université de Toulouse, 14 avenue Edouard Belin, 31400 Toulouse, France

November 24, 2018, *Revision* : 1.149, accepted for publication in A&A

ABSTRACT

Context. Hydrodynamical model of the κ -mechanism in a purely radiative case.

Aims. First, to determine the physical conditions propitious to κ -mechanism in a layer with a configurable conductivity hollow and second, to perform the (nonlinear) direct numerical simulations (DNS) from the most favourable setups.

Methods. A linear stability analysis applied to radial modes using a spectral solver and DNS thanks to a high-order finite difference code are compared.

Results. Changing the hollow properties (location and shape) lead to well-defined instability strips. For a given position in the layer, the amplitude and width of the hollow appear to be the key parameters to get unstable modes driven by κ -mechanism. The DNS achieved from these more auspicious configurations confirm the growth rates as well as structures of linearly unstable modes. The nonlinear saturation follows through intricate couplings between the excited fundamental mode and higher damped overtones.

Key words. Hydrodynamics - Instabilities - Waves - Stars: oscillations - Methods: numerical

1. Introduction

Since the beginning of the studies concerning Cepheids, it is well known that convection occurs in Cepheids' envelopes, and thus changes pulsation properties (e.g. the reviews of Gautschy & Saio 1996; Buchler 1997). The coldest ones, which are located next to the red edge of the instability strip, have the more extended surface convective zones. However, during many years Cepheids' oscillations models have used the so-called "frozen-in convection" approximation which claims that convective flux perturbations are negligible (Baker & Kippenhahn 1962). Such kind of models well predict the blue edge of the instability strip but fail to explain the red edge as in this case, the strong existing couplings between the convection and the oscillations are not taken into account. This discrepancy becomes obvious with the accumulation of accurate observations which show a narrower instability strip than the theoretical one, i.e. modes which are linearly unstable in the models are located outside the observational strip (Yecko et al. 1998, hereafter YKB98).

The main theoretical difficulty comes from the fact that convection plays a crucial role on the pulsations while we know that convection itself remains roughly described by mixing-length theories (Vitense 1953; Böhm-Vitense 1958). However, several attempts in the direction of time dependent convection models (TDC) have been developed (e.g. Unno 1967; Gough 1977; Stellingwerf 1982). Recent studies (YKB98; Bono et al. 1999) rely on Stellingwerf's convection model (Stellingwerf 1982) or very similar newer approaches to compute linear and nonlinear time evolution of

amplitudes of modes (Kuhfuß 1986; Gehmeyr & Winkler 1992; Wuchterl & Feuchtinger 1998). The major problem of TDC is the choice of the many free parameters introduced by the convection model¹. As these parameters are not theoretically well determined, one should adjust them by fitting the observations.

Another way to study the convection-pulsation interaction is to achieve (nonlinear) direct numerical simulations (DNS) of the whole hydrodynamical problem. The final aim of our work is to realise such kind of simulations in 2-D and 3-D where a convective zone will be coupled with a radiative one and unstable radial acoustic modes will be self-consistently excited by κ -mechanism. However, as DNS are highly time consuming, it is necessary to get in a first step the appropriate initial conditions. That is why we have tried to determine in this paper the physical conditions propitious to an excitation based on κ -mechanism.

Eddington (1917), and then Zhevakin (1953) and Cox (1958) have introduced a mechanism linked to the opacity in ionisation regions, the κ -mechanism, where κ denotes opacity (see also the review of Zhevakin 1963). They have shown that Cepheids' radial oscillations are driven by a thermal heat engine as radial pulsations have to be maintained thanks to a sustained physical process. That is why, they imagined a Carnot-like thermodynamic cycle which stores heat during compression phases while releasing it during the decompression ones. This mechanism, now called the *Eddington's valve*, can only occur in specific regions of a star where the opacity varies so as to block the radiative flux during compression phases. Now, opacity tables

¹ e.g. the seven coefficients [α_c , α_t , α_ν , α_Λ , α_s , α_d , α_p] in YKB98 or the eight ones in Kolláth et al. (2002).

such as the OPAL ones show strong increases in ionisation regions of main (i.e. Hydrogen and Helium) or heavy elements that are commonly called “ionisation bumps” (e.g. Seaton & Badnell 2004). As a consequence these ionisation zones are locally responsible for modes amplification. Moreover, beyond this criterion on opacity, these ionisation regions have to be located in a very precise region of a star.

Indeed, if they are too deep or too close to the surface, the driving they cause can be balanced by the damping occurring in other regions. Therefore, an efficient ionisation region has to be located in a specific place, called the *transition region*, which marks the shift from a quasi-adiabatic interior to a strongly non-adiabatic surface. In classical Cepheids oscillating on the radial fundamental mode, the overlap of this transition region with the ionisation one is around 40 000 K, which corresponds to the temperature of the helium second ionisation (Baker & Kippenhahn 1965). For first overtone Cepheids, things are more intricate as one must take into account first, the respective position between this HeII ionisation region and the nodal line and second, the HeI/H region which also contributes to the driving (Bono et al. 1999).

However, the location of these opacity bumps are not solely responsible of the acoustic mode destabilisation. A careful treatment of the κ -mechanism in Cepheid stars would also involve the possible dynamical couplings with convective zones or, say, metallicity effects through a realistic equation of state and opacity tables. The corresponding physics is actually not fully understood from a theoretical point of view and the purpose of our work is to sufficiently simplify the hydrodynamical approach while keeping at the same time the *leading order* phenomenon responsible of the instability, that is, the opacity bumps location.

That’s for why we adopt a fully radiative layer of a perfect gas in which a ionisation region is represented by a “hollow” in radiative conductivity, corresponding to a “bump” in opacity. Strictly speaking, the layer stability will depend on both temperature and density variations, as the radiative conductivity is a function of these two physical quantities. However, as the opacity strongly depends on temperature, this state variable mainly controls the instability. As our final aim is to realise an hydrodynamical study of κ -mechanism, we will therefore neglect any dependence of radiative conductivity on density and thus, our conductivity profile is merely a function of temperature. The inferred advantage is to allow easy changes in the different parameters of the ionisation region by setting both position and shape of the conductivity hollow (i.e. its slope, width and amplitude). As a consequence, it is possible to investigate a complete parametric study of κ -mechanism in order to determine precisely the physical conditions required by the instability.

We first consider the radiative and hydrostatic equilibria of our layer with an appropriate conductivity profile. By adjusting both the density value at the top of the layer and the flux at its bottom, we then obtain a transition region in the middle of the computational domain. Secondly, we investigate the linear stability analysis by solving perturbation equations for the oscillations. We thus obtain the whole spectrum, and can sort out unstable modes from stable ones. Therefore, we are able to check the relevance of the transition region concept by making every parameters of the conductivity hollow vary.

The first main result of our linear stability study is the confirmation of the underlying conditions defining the transition region. With different parametric studies, we obtain instability strips corresponding to the fundamental mode, as both a minimum hollow width and amplitude are needed to obtain unstable modes. These results are interpreted thanks to the work integral to exactly determine the location of the driving zone. As a consequence, this parametric study of κ -mechanism provides us the physical quantities responsible for the instability.

Secondly, these auspicious conditions needed to drive the fundamental mode constitute the starting point of 2-D DNS. Indeed, we check the growth rates as well as the structure of the linearly unstable modes by performing direct simulations until the nonlinear saturation of modes.

In §2, we first introduce the general oscillation equations while the different conditions leading to the instability are determined in §3. In §4, we present our hydrodynamical model. Linear stability analysis and DNS results are thus given and compared in §5 and §6, respectively, before concluding in §7.

2. The general oscillations equations

Our system is composed by a 2-D plane parallel layer of width d . z denotes a cartesian coordinate, pointing upward on the contrary of the constant gravity field \mathbf{g} . The gas is assumed to be monatomic and perfect, so its equation of state is given by

$$p = R_* \rho T \quad \text{and} \quad \gamma \equiv \frac{c_p}{c_v} = \frac{5}{3}, \quad (1)$$

where p , ρ and T respectively denote pressure, density and temperature, R_* is the ideal gas constant and γ the ratio of specific heats c_p and c_v .

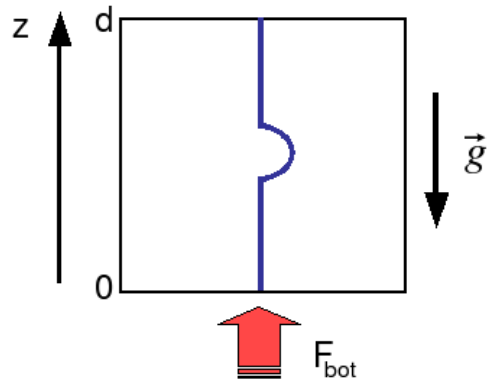


Fig. 1. Scheme corresponding to our model. Gravity is pointing downward, contrary to the vertical coordinate. The (blue) curve represents the radiative conductivity profile that we are going to discuss further whereas large (red) arrow expresses the radiative flux entering in the bottom of the layer.

We are interested in small perturbations around an equilibrium state, that is, any physical quantity is expanded around its mean value $X_0(\mathbf{r})$ as

$$X(\mathbf{r}, t) = X_0(\mathbf{r}) + X'(\mathbf{r}, t) \quad \text{with} \quad X'/X_0 \ll 1, \quad (2)$$

where X' is an Eulerian perturbation. Linearized continuity, momentum and energy equations for the perturbations in a non-adiabatic case are given by (e.g. Unno et al. 1989)

$$\left\{ \begin{array}{l} \lambda \rho' = -\rho_0 \operatorname{div} \mathbf{u} - \mathbf{u} \cdot \nabla \ln \rho_0 \\ \lambda \mathbf{u} = -\frac{1}{\rho_0} \nabla p' + \frac{\rho'}{\rho_0} \mathbf{g} \\ \quad + \nu \left(\Delta \mathbf{u} + \frac{1}{3} \nabla \operatorname{div} \mathbf{u} + 2\mathbf{S} \cdot \nabla \ln \rho_0 \right) \\ \lambda T' = -\frac{1}{\rho_0 c_v} \operatorname{div} \mathbf{F}' - (\gamma - 1) T_0 \operatorname{div} \mathbf{u} - \mathbf{u} \cdot \nabla T_0, \end{array} \right. \quad (3)$$

where \mathbf{u} , ρ' , T' and \mathbf{F}' denote the velocity, density, temperature and radiative flux perturbations, respectively. The kinematic viscosity ν is supposed to be constant and \mathbf{S} denotes the traceless rate-of-strain tensor given by

$$S_{ij} = \frac{1}{2} \left(\frac{\partial u_i}{\partial x_j} + \frac{\partial u_j}{\partial x_i} - \frac{2}{3} \delta_{ij} \operatorname{div} \mathbf{u} \right). \quad (4)$$

We seek normal modes with a time-dependence of the form $\exp(\lambda t)$, where $\lambda = \tau + i\omega$. The real part τ denotes the growing ($\tau > 0$) or damping ($\tau < 0$) rate whereas the imaginary part ω denotes the frequency. We now assume that the layer is fully radiative which, under the diffusion approximation, leads to the following expression of the radiative flux perturbation

$$\mathbf{F}' = -K_0 \nabla T' - K' \nabla T_0, \quad (5)$$

where K_0 denotes the radiative conductivity and K' its Eulerian perturbation. This perturbation K' can be related in a general way to the temperature one by

$$\frac{K'}{K_0} = \mathcal{K}_T \frac{T'}{T_0} \quad \text{with} \quad \mathcal{K}_T = \frac{d \ln K_0}{d \ln T_0}. \quad (6)$$

Finally, we impose the following boundary conditions

$$\left\{ \begin{array}{l} u_z = 0 \quad \text{for} \quad z = [0, d], \\ \frac{dT'}{dz} = 0 \quad \text{for} \quad z = 0 \quad \text{and} \quad T' = 0 \quad \text{for} \quad z = d, \end{array} \right. \quad (7)$$

which correspond to rigid walls at both limits of the domain, a perfect conductor at the bottom and a perfect insulator at the top.

3. Conditions for instability

3.1. A first condition derived from the work integral

We recall that the main aim of this work is to clarify the favourable conditions which may sustain unstable radial modes in a plane parallel layer. An advisable mean to study the physics of such instability is the work integral. In the following, we are going to assume that transformations are quasi-adiabatic. This approximation is sufficient in the deeper layers of a star but becomes no longer valid near its surface where non-adiabatic effects dominate. Nevertheless, this approximation is useful when one wants to have an idea of the stability properties of an oscillation mode.

Using the work integral formalism in the quasi-adiabatic limit, we demonstrate in Appendix A.1 the following expression for the damping or growing rate of an eigenmode

$$\tau = -\frac{\Re \left[\int_V (\gamma - 1) \frac{\delta \rho^*}{\rho} \operatorname{div} \mathbf{F}' dV \right]}{\int_V |\mathbf{u}|^2 \rho_0 dV}, \quad (8)$$

where the symbol \Re means the real part. We thus see that the sign of τ only depends on the numerator which, under the diffusion approximation, Eq. (5), leads to

$$\tau \propto \Re \left[\int_0^d \frac{\delta \rho^*}{\rho_0} \operatorname{div} (K' \nabla T_0 + K_0 \nabla T') dz \right]. \quad (9)$$

The main driving term in this expression is $K' \nabla T_0$ because it represents the dynamical variation of opacity during an oscillation cycle, which is the cause of κ -mechanism. We thus neglect $K_0 \nabla T'$ to get

$$\tau \propto \Re \left[\int_0^d \frac{\delta \rho^*}{\rho_0} \operatorname{div} (K' \nabla T_0) dz \right]. \quad (10)$$

As we can see in Fig. 3b, the equilibrium temperature is an almost linear function of z , except in the vicinity of the conductivity hollow. Therefore, ∇T_0 is almost constant thus we have

$$\tau \propto \Re \left[\int_0^d \frac{\delta \rho^*}{\rho_0} \nabla T_0 \nabla K' dz \right]. \quad (11)$$

With Eq. (6), we have $K' = K_0(T_0) \mathcal{K}_T T' / T_0$. As we are interested in low order modes we assume that $\nabla K'$ is dominated by $K_0(T_0) T' / T_0 \nabla \mathcal{K}_T$. The same approximation will be done in Eq. (17). We then obtain

$$\tau \propto \Re \left[\int_0^d \frac{\delta \rho^*}{\rho_0} \nabla T_0 K_0(T_0) \frac{T'}{T_0} \nabla \mathcal{K}_T dz \right]. \quad (12)$$

Let us now consider a compression phase corresponding to $\delta \rho^* / \rho_0 > 0$ and $T' / T_0 > 0$. As $\nabla T_0 < 0$, a necessary condition to obtain unstable modes with $\tau > 0$ is then

$$\frac{d\mathcal{K}_T}{dz} < 0. \quad (13)$$

In variable stars, this condition can occur in ionisation regions. Indeed, opacity tables clearly show that these regions are associated with large ‘‘bumps’’ in opacity (e.g. the review of Carson 1976; Seaton & Badnell 2004). With Eq. (13), one can obtain unstable modes if driving prevails over damping. This result has the following physical meaning: if the radiative conductivity decreases during a compression phase, then some part of the radiative flux is blocked and some energy is stored during compression contributing to increase the ratio of ionised matter. During the decompression phase, this extra energy is released under mechanical work to the environment and can excite the oscillations. It works as Eddington predicted when he imagined a thermal heat engine to justify Cepheids’ oscillations (Eddington 1917).

3.2. A second condition derived from the so-called “transition region”

In the previous paragraph, we have recalled a necessary condition to obtain unstable modes (Eq. 13). Nevertheless, the demonstration was made under the quasi-adiabatic approximation which fails near the surface. As a consequence, we cannot know if the driving caused by ionisation regions can prevail over other damping regions. Indeed, ionisation regions where Eq. (13) is satisfied are very thin compared to the whole atmosphere of a star and thus the influence of the damping regions on the instability remains questioning at this stage. Hereafter, we will essentially follow Cox’s demonstration (e.g. Cox 1980; Christensen-Dalsgaard 2003).

In Lagrangian variables, the energy equation can be written as

$$\frac{d}{dt} \left(\frac{\delta T}{T_0} \right) - (\gamma - 1) \frac{d}{dt} \left(\frac{\delta \rho}{\rho_0} \right) = - \frac{F_{\text{bot}}}{\rho_0 c_v T_0} \text{div} \left(\frac{F'}{F_{\text{bot}}} \right), \quad (14)$$

where the symbol δ means Lagrangian perturbations. As we consider a 1-D box, we simply have

$$-d \left(\frac{F'}{F_{\text{bot}}} \right) dt = \frac{\rho_0 c_v T}{F_{\text{bot}}} d \left[\frac{\delta T}{T_0} - (\gamma - 1) \frac{\delta \rho}{\rho_0} \right] dz. \quad (15)$$

Let us integrate between a given height z and the surface to get

$$\Delta \left(\frac{F'}{F_{\text{bot}}} \right) \Pi \sim \frac{\langle c_v T_0 \rangle}{F_{\text{bot}}} \int_z^d \rho_0 dz' d \left[\frac{\delta T}{T_0} - (\gamma - 1) \frac{\delta \rho}{\rho_0} \right], \quad (16)$$

where $\Delta(F'/F_{\text{bot}})$ is the variation of F'/F_{bot} between the considered point and the surface, $\langle c_v T_0 \rangle$ is an average of $c_v T_0$ over this region and Π is a characteristic dynamical timescale (the pulsation period of the fundamental mode, typically). As we are principally interested in the study of low order modes (i.e. the fundamental one), we assume that the eigenvectors are almost constant (e.g. Cox 1980). As a consequence, one obtains

$$d \left[\frac{\delta T}{T_0} - (\gamma - 1) \frac{\delta \rho}{\rho_0} \right] \approx \left\langle \frac{\delta T}{T_0} - (\gamma - 1) \frac{\delta \rho}{\rho_0} \right\rangle_z, \quad (17)$$

where $\langle \cdot \rangle_z$ expresses an average of the eigenfunctions. Noting that

$$\int_z^d \rho_0 dz' = \frac{\Delta m}{S} \quad \text{and} \quad L = F_{\text{bot}} S, \quad (18)$$

leads to

$$\Delta \left(\frac{F'}{F_{\text{bot}}} \right) \sim \Psi \left\langle \frac{\delta T}{T_0} - (\gamma - 1) \frac{\delta \rho}{\rho_0} \right\rangle_z, \quad (19)$$

where

$$\Psi = \frac{\langle c_v T_0 \rangle \Delta m}{\Pi L}. \quad (20)$$

Ψ has the following physical meaning: it represents the ratio of the thermal energy embedded between the considered point and the surface to the energy radiated during an oscillation period². A second instability criterion can then be derived from the value of this quantity Ψ :

² Ψ can also be interpreted as the ratio of the local thermal timescale to the dynamical one.

- If the considered point is too deep in the star, the local thermal timescale is longer than the dynamical one and $\Psi \gg 1$. As a consequence, pulsation has no influence on the energy release and the adiabatic approximation³ is well-suited in this case.
- On the contrary, if the considered point is next to the surface, then Δm is very small and $\Psi \ll 1$. As a consequence, the energy content (and the corresponding mass content) is too weak to influence the radiative flux and the luminosity perturbation is said to be *frozen in*. It means that the radiative flux perturbation doesn’t vary anymore in this region.
- Between these two regions, Ψ can be $\mathcal{O}(1)$ which defines a zone called the *transition region* separating the adiabatic interior from the strongly non-adiabatic surface, that is,

$$\Psi = \frac{\langle c_v T_0 \rangle \Delta m}{\Pi L} \sim 1. \quad (21)$$

King & Cox (1968) have first determined the temperature associated with this transition region for different Cepheids’ models. For the fundamental mode, they have obtained $T_{\text{TR}} \simeq 40\,000$ K while the transition lies nearer the surface for higher order modes.

The corresponding positions of ionisation regions and transition ones are therefore crucial for the instability (Gilliland et al. 1998). Indeed, if they overlap -it corresponds to the instability strip- the bottom of the ionisation region strongly contributes to driving because it acts in a quasi-adiabatic place. On the contrary, its top is in a strongly non-adiabatic region where the luminosity is frozen in. As a consequence, the zone over ionisation region is not damping and driving prevails in this case: modes become unstable (see e.g. Cox (1980) for a more detailed description).

We then sum up the conditions propitious to instability as

$$\frac{d\mathcal{K}_T}{dz} < 0 \quad \text{and} \quad T_{\text{TR}} \sim T_{\text{ionisation}}. \quad (22)$$

With the conditions given in Eq. (22), one thus obtains $T_{\text{ionisation}} \simeq 40\,000$ K. This temperature corresponds to the second Helium ionisation which is known to be mainly responsible for the driving of modes in Cepheids (see Cox 1963).

4. Our hydrodynamical model

4.1. The choice of the radiative conductivity profile

Strictly speaking, radiative conductivity K_0 depends both on temperature and density as diffusion approximation gives (e.g. Mihalas & Weibel Mihalas 1984)

$$K_0 = \frac{16\tilde{\sigma}T^3}{3\kappa\rho}, \quad (23)$$

where $\tilde{\sigma}$ denotes Stefan-Boltzmann’s constant. Kramer’s laws constitute good approximations of opacity laws with

³ One can notice that the “adiabatic” approximation means here that deeply in the layer the mode has an adiabatic behaviour whereas next to the surface it remains strongly non-adiabatic.

$$\kappa \propto \rho^n T^{-s}, \quad (24)$$

where, for example, $n = 1$ and $s = 3.5$ for the free-free opacity (e.g. Hansen & Kawaler 1994). As shown in the Introduction and in §2, we simply consider here a constant radiative conductivity on which a hollow representing a bump in opacity is added. This simple approach is an easy way to reproduce the physical conditions propitious to κ -mechanism while keeping the ability to quickly change the hollow amplitude, slope or width and achieving so an efficient parametric study of the instability. As a consequence, the radiative conductivity is given by⁴

$$K_0(T) = K_{\max} \left[1 + \mathcal{A} \frac{-\pi/2 + \arctan(\sigma T^+ T^-)}{\pi/2 + \arctan(\sigma e^2)} \right], \quad (25)$$

with

$$\mathcal{A} = \frac{K_{\max} - K_{\min}}{K_{\max}}, \quad T^\pm = T - T_{\text{bump}} \pm e, \quad (26)$$

and

- T_{bump} is the position of the hollow in temperature.
- K_{\max} and K_{\min} are the conductivity extrema, \mathcal{A} being the corresponding relative amplitude.
- σ represents the slope of the hollow.
- e represents the half of the full width at half maximum (i.e. FWHM/2) of the hollow.

Examples of common values of these parameters are given in Fig. 2.

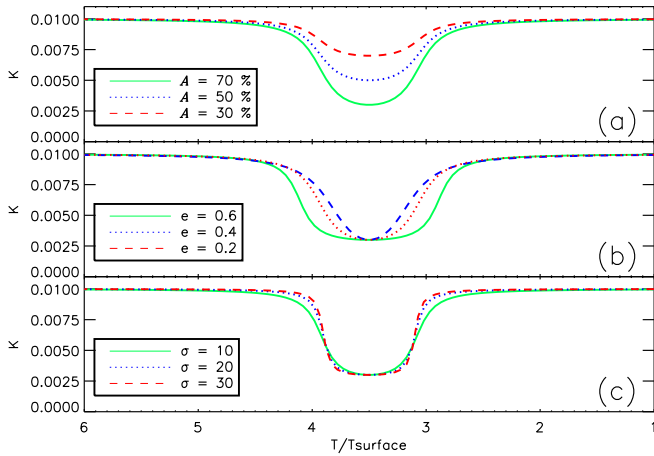


Fig. 2. Influence of the hollow parameters on the conductivity profile for $K_{\max} = 10^{-2}$ and $T_{\text{bump}} = 3.5$: amplitude \mathcal{A} (a), width e (b) and slope σ (c) (here the abscissa denotes a dimensionless temperature based on the surface one, i.e. T/T_{surface})

⁴ This arctan-profile may appear quite intricate, compared e.g. to a gaussian-like one, but it allows us to change almost independently the hollow parameters (i.e. changing its amplitude while keeping its width).

4.2. The equilibrium setup

Hydrostatic and radiative equilibria in the diffusion limit are given by

$$\begin{cases} \nabla p_0 = \rho_0 g \\ \text{div} [K_0(T_0) \nabla T_0] = 0. \end{cases} \quad (27)$$

Assuming a constant radiative flux F_{bot} at the bottom of the layer leads to

$$\begin{cases} \frac{dp_0}{dz} = -\rho_0 g \\ \frac{dT_0}{dz} = -\frac{F_{\text{bot}}}{K_0}. \end{cases} \quad (28)$$

Let us choose the depth of the layer d as the length scale and the temperature at the top of the layer T_{top} as the temperature scale, i.e. $[z] = d$ and $[T] = T_{\text{top}}$. Moreover, the top density is chosen as the density scale ($[\rho] = \rho_{\text{top}}$), velocity is given in units of $\sqrt{c_p T_{\text{top}}}$, gravity in units of $c_p T_{\text{top}}/d$, pressure in units of $\rho_{\text{top}} [u^2]$, while radiative conductivity is given in units of $\rho_{\text{top}} c_p d [u]$. Corresponding radiative flux unit is then $\rho_{\text{top}} (c_p T_{\text{top}})^{3/2}$. The dimensionless equations then become

$$\begin{cases} \frac{d \ln \tilde{p}_0}{dz} = -\frac{\gamma}{\gamma - 1} \frac{\tilde{g}}{\tilde{T}_0} \\ \frac{d \tilde{T}_0}{dz} = -\frac{\tilde{F}_{\text{bot}}}{\tilde{K}_0} \\ \tilde{p}_0 = \frac{\gamma - 1}{\gamma} \tilde{\rho}_0 \tilde{T}_0. \end{cases} \quad (29)$$

The set of equations (29) can be written in matrix form as

$$A \psi = B(\psi), \quad (30)$$

where $\psi = (p_0, T_0)^T$ is the equilibrium field vector and A, B are differential operators. One notes that the RHS, $B(\psi)$, depends on the eigenvector itself through the terms $1/\tilde{T}_0$ and $1/\tilde{K}_0(\tilde{T}_0)$, which means solving a *nonlinear* problem.

Finally, tildes on equilibrium fields emphasise dimensionless quantities but they will be dropped for clarity in the following.

4.3. About Schwarzschild's criterion in our model

It is important to keep our box entirely radiative. That is why, we must take care of Schwarzschild's criterion (e.g. Chandrasekhar 1961)

$$\left| \frac{dT_0}{dz} \right| < \left| \frac{dT_0}{dz} \right|_{\text{adia}} \quad \text{with} \quad \left| \frac{dT_0}{dz} \right|_{\text{adia}} = \frac{g}{c_p}. \quad (31)$$

If this inequality is ensured, then the layer is fully radiative. In our dimensionless units, this condition becomes

$$\left| \frac{dT_0}{dz} \right| < g, \quad (32)$$

meaning that large variations in temperature through the domain necessarily require large values for the dimensionless gravity field g .

4.4. Back to the radial oscillations equations

To simplify the general system of oscillations equations (3) we first define the following new variables

$$R \equiv \rho'/\rho_0 \quad \text{and} \quad \theta \equiv T'/T_0. \quad (33)$$

Then, by using Eq. (29) and substituting the conductivity equation into the energy one (see Appendix B), one gets

$$\left\{ \begin{array}{l} \lambda R = -\operatorname{div} \mathbf{u} - \mathbf{u} \cdot \nabla \ln \rho_0 \\ \lambda \mathbf{u} = -\frac{p_0}{\rho_0} \nabla(\theta + R) - \theta \mathbf{g} \\ \quad + \nu \left(\Delta \mathbf{u} + \frac{1}{3} \nabla \operatorname{div} \mathbf{u} + 2\mathbf{S} \cdot \nabla \ln \rho_0 \right) \\ \lambda \theta = \frac{1}{\rho_0 c_v T_0} \Delta_z (K_0 T_0 \theta) - (\gamma - 1) \operatorname{div} \mathbf{u} - \mathbf{u} \cdot \nabla \ln T_0, \end{array} \right. \quad (34)$$

We then adopt the same dimensionless quantities used in the equilibrium equations (29)

$$\left\{ \begin{array}{l} \lambda R = -\frac{du_z}{dz} - \frac{d \ln \rho_0}{dz} u_z \\ \lambda u_z = -\frac{\gamma - 1}{\gamma} T_0 \left(\frac{dR}{dz} + \frac{d\theta}{dz} \right) + g\theta + \mathcal{D}_\nu \\ \lambda \theta = \gamma \chi_0 \left[\frac{d^2 \theta}{dz^2} + 2 \left(\frac{d \ln K_0}{dz} + \frac{d \ln T_0}{dz} \right) \frac{d\theta}{dz} \right. \\ \quad \left. + \frac{d \ln T_0}{dz} \frac{dK_T}{dz} \theta \right] - (\gamma - 1) \frac{du_z}{dz} - \frac{d \ln T_0}{dz} u_z, \end{array} \right. \quad (35)$$

where u_z denotes the vertical velocity, $\chi_0 = K_0/\rho_0 c_p$ the radiative diffusivity and the viscous dissipative term \mathcal{D}_ν is given by

$$\mathcal{D}_\nu = \frac{4}{3} \nu \left(\frac{d^2 u_z}{dz^2} + \frac{d \ln \rho_0}{dz} \frac{du_z}{dz} \right). \quad (36)$$

This system (35) may formally be written as a generalised eigenvalue problem

$$A\psi = \lambda B\psi, \quad (37)$$

where $\lambda = \tau + i\omega$ is the complex eigenvalue associated with the eigenvector $\psi = (R, u_z, \theta)^T$ while A , B denote differential operators.

Finally the set of boundary conditions (7) written for (u_z, θ) is

$$\left\{ \begin{array}{l} u_z = 0 \quad \text{for } z = [0, 1] \\ \frac{d\theta}{dz} + \frac{d \ln T_0}{dz} \theta = 0 \quad \text{for } z = 0 \\ \theta = 0 \quad \text{for } z = 1. \end{array} \right. \quad (38)$$

4.5. The numerical methods

We solve the two linear algebra problems (30) and (37-38) using the LSB code (Linear Solver Builder, Valdetaro et al. 2007). Both problems are discretized on the Gauss-Lobatto grid associated with Chebyshev's polynomials leading to two distinct numerical problems:

1. *the equilibrium model*: the computation of the equilibrium structure requires to solve a *nonlinear* problem. One way to do that is to use the so-called ‘‘Picard’s method’’ based on the fixed-point algorithm (Hairer et al. 1993; Fukushima 1997). It consists in solving our set of first-order ordinary differential equations by successive iterations, that is, we advance

$$A\psi_{n+1} = B(\psi_n). \quad (39)$$

This scheme converges quite well provided that the initial guess ψ_0 is not ‘‘too far’’ from the solution and that nonlinearities are weak.

2. *the eigenmodes*: we can compute the whole spectrum of complex eigenvalues λ using the QZ algorithm (Moler & Stewart 1973) or just compute a pair (λ, ψ) around a given guess of λ using the iterative Arnoldi-Chebyshev algorithm (Arnoldi 1951; Saad 1992).

5. Results

In Eq. (32), we have shown that the temperature contrast across the layer (and also the associated density and pressure ones) is limited by the gravity field g . It may however be judicious not to restrict ourselves to small density contrasts as the mass involved between the conductivity hollow and the surface, that is Δm , enters in one of the two favourable criteria for the instability, see Eq. (21). We will therefore consider in the following a ‘‘convenient’’ value $g = 7$.

Moreover, we have to keep as small as possible the radiative conductivity as we want to avoid too large values of diffusivity χ_0 , that is, we do not want to deviate too much from conditions of the applying of quasi-adiabatic developments. We therefore choose $K_{\max} = 10^{-2}$. As a consequence, the system (29) combined with Schwarzschild’s criterion (32) restrict the possible values of the imposed bottom flux and we thus set $F_{\text{bot}} = 2 \times 10^{-2}$ in the following. Using mild spatial resolutions, we choose a conservative value for the kinematic viscosity, that is, $\nu = 5 \times 10^{-4}$.

5.1. Computation of equilibrium fields

To compute the equilibrium fields from second-order system (29), we must choose two different boundary conditions, one on temperature and one on pressure. Without loss of generality, we first set $T_0 = 1$ at the top of the layer. Second, as we are interested in having the transition region of the fundamental mode located in the layer middle, Eq. (21) has to be satisfied at that place. We have already said that $F_{\text{bot}} = 2 \times 10^{-2}$ and $K_{\max} = 10^{-2}$. Temperature value is fixed by F_{bot} , K_{\max} and its boundary condition. The pulsation period of the fundamental mode is roughly expressed by

$$\Pi \simeq \frac{2d}{\langle c_s \rangle}, \quad (40)$$

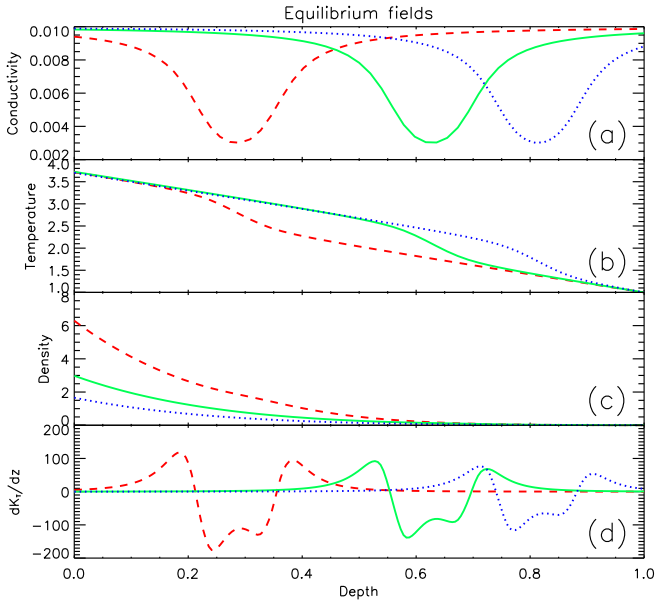


Fig. 3. **a)** Three different conductivity hollows: $T_{\text{bump}} = 2.8$ (dashed red line), $T_{\text{bump}} = 2.1$ (solid green line) and $T_{\text{bump}} = 1.7$ (dotted blue line), with $\mathcal{A} = 70\%$, $e = 0.4$ and $\sigma = 7$; **b)** corresponding temperature profiles; **c)** density profiles; **d)** equilibrium profiles for $d\mathcal{K}_T/dz$.

where $\langle c_s \rangle$, denoting the mean sound speed, is related to the temperature contrast across the layer. Thus, the only parameter that we can change in Eq. (21) is Δm . This value is directly linked to the boundary condition on density. In order to have a suitable Δm -value in the box middle, we therefore decide to take $\rho_0 = 2.5 \times 10^{-3}$ at the top of the layer (corresponding to $\ln P_0 = -6.9$).

Once chosen the values of the hollow parameters - T_{bump} , \mathcal{A} , e and σ - we then solve the problem (29) on the Gauss-Lobatto grid to obtain the three equilibrium fields T_0 , P_0 and ρ_0 . With these fields, it is possible to compute any physical quantities needed in the oscillations equations (35), e.g. \mathcal{K}_T or the diffusivity χ_0 . Some examples of obtained equilibrium fields are given in Fig. 3 for three different positions of the conductivity hollow.

5.2. Computation of eigenmodes

With the different equilibrium quantities, we solve the eigenvalue problem (35) to get the whole spectrum of eigenvalues λ . Among them, it is possible to obtain the nearest eigenvalue from a guessed one using the iterative Arnoldi-Chebyshev algorithm. As an example, Fig. 4 brings out the eigenfunctions associated with the unstable fundamental mode.

In order to check the convergence of this mode, we also compute the spectra corresponding to the different eigenfunctions, see Fig. 5.

Finally, in order to determine the influence of the conductivity hollow on that fundamental eigenvector, we compute three eigenmodes with the different values of T_{bump} previously used in Fig. 3. The result is displayed in Fig. 6 for the temperature perturbation θ , where the case of a constant radiative conductivity profile (i.e. without a conductivity hollow) is superimposed:

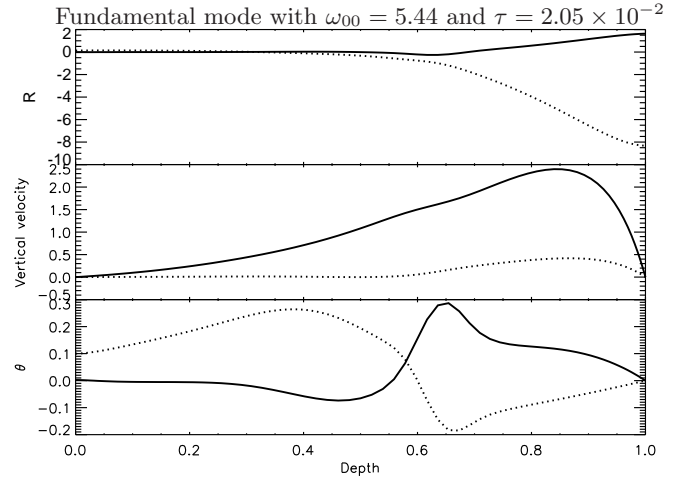


Fig. 4. Eigenfunctions (R , u_z , θ) for the unstable fundamental mode, corresponding to a hollow with $T_{\text{bump}} = 2.1$, $\mathcal{A} = 70\%$, $e = 0.4$ and $\sigma = 7$. The equilibrium setup used to compute this mode is the one displayed by a solid green line in Fig. 3.

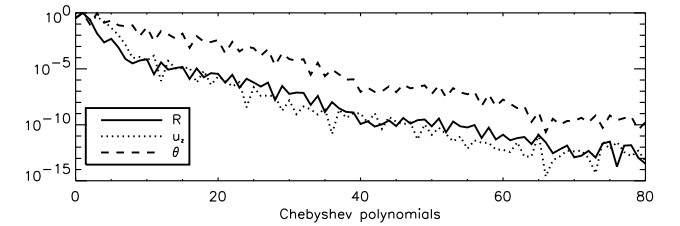


Fig. 5. Chebyshev's spectra of the different fields (R , u_z , θ) for the eigenmode shown in Fig. 4. Spectral precision is reached for every field.

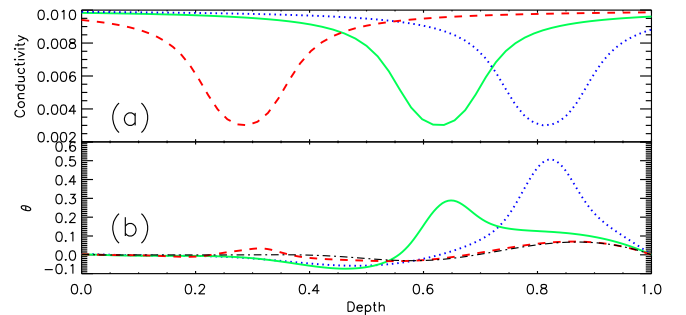


Fig. 6. **a)** Three different conductivity profiles with $T_{\text{bump}} = 1.7$ (dotted blue line), $T_{\text{bump}} = 2.1$ (solid green line) and $T_{\text{bump}} = 2.8$ (dashed red line); **b)** corresponding fundamental eigenmodes (here the real part of temperature perturbations θ). The case with a constant radiative conductivity $K_0(T_0) = K_{\text{max}}$ is superimposed as a dot-dashed black line.

- The first case, corresponding to the dotted (blue) line, denotes a hot star where the ionisation region is close to the surface. The conductivity hollow has an influence on the temperature eigenfunction which is strongly deformed at its location. We will show in §5.4 that this de-

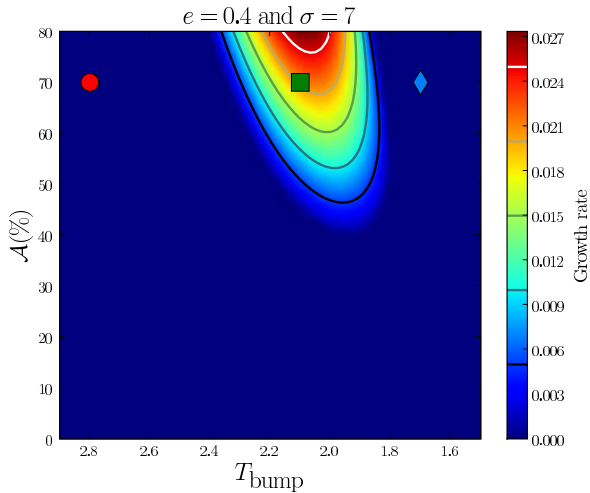


Fig. 7. Instability strip for the fundamental mode in the plane $(T_{\text{bump}}, \mathcal{A})$ for given values of e and σ (isocontours in growth rates τ are displayed). The three marks correspond to the three particular computations done in Figs. 3 and 6 for $T_{\text{bump}} = 1.7$ (blue diamond, stable), $T_{\text{bump}} = 2.1$ (green square, unstable) and $T_{\text{bump}} = 2.8$ (red circle, stable).

formation is not sufficient to destabilise this mode as the Ψ -criterion should also be taken into account (Eq. 21).

- The second one, corresponding to the solid (green) line, emphasises a case where ionisation occurs approximately in the middle of the layer. The eigenvector is still deformed by the conductivity hollow.
- The last case, corresponding to the dashed (red) line, denotes a cold star where ionisation region is far from the surface. For this hollow location, the dynamical timescale is very small compared to the local thermal one. As a consequence, thermodynamic transformations are quasi-adiabatic and non-adiabatic effects are negligible *there*. This is confirmed in Fig. 6b where the eigenmode is practically not deformed by the conductivity hollow. To enlighten this result, we have superimposed the case corresponding to a constant radiative conductivity ($K_0(T_0) = K_{\text{max}}$). The obtained temperature perturbations (the dot-dashed (black) line) are really next to the dashed (red) one, meaning that the hollow has a marginal effect on the mode stability.

We then show that the conductivity hollow has only an influence on the shape of the eigenmode in upper parts of our layer. In deeper regions, adiabatic thermodynamic transformations are overwhelming and the eigenvector is pretty unchanged by the variations in the conductivity profile.

5.3. Parametric surveys of the instability

As claimed in §4.1, our conductivity profile is well-suited to deal with a parametric study of the κ -mechanism, as its parameters T_{bump} , \mathcal{A} , e and σ can easily be changed. We thus next introduce the three parametric surveys which allowed us to find the instability strips associated with the κ -mechanism.

5.3.1. The $T_{\text{bump}} - \mathcal{A}$ survey

At first, we want to determine the influence of the hollow amplitude on stability. As a consequence, we choose a value for σ and e and make T_{bump} and \mathcal{A} vary. For each value of these two parameters, we compute first the equilibrium fields and then, the eigenvalues with their corresponding eigenvectors. Unstable modes are extracted among all eigenvalues as their growth rate are positive. Fig. 7 displays the obtained instability strip:

- Dark (blue) areas correspond to stable fundamental modes (i.e. with $\tau < 0$).
- Coloured areas correspond to unstable fundamental modes with the lighter the colour the bigger the growth rate.

Two major results can then be derived from this figure: (i) a particular region in our layer ($T_{\text{bump}} \in [1.8, 2.3]$) seems to be propitious to the appearance of unstable modes, that is, one recovers the concept of transition region discussed in §3.2; (ii) a minimal amplitude in the hollow is required to get an instability ($\mathcal{A}_{\text{min}} \simeq 45\%$).

5.3.2. The $T_{\text{bump}} - \sigma$ survey

Next, we study the influence of the slope σ of the conductivity hollow on stability. We thus choose a value for the amplitude \mathcal{A} and width e while making T_{bump} and σ vary. As for the previous survey, we plot in Fig. 8 the isocontours in growth rates τ but now in the plane $(T_{\text{bump}}, \sigma)$.

We then found the same kind of areas than in Fig. 7, that is, an instability strip where modes are unstable (e.g. the coloured region) embedded in large (dark) regions where modes are stable. Nevertheless, the influence of the slope σ on stability is less significant than the amplitude one. In fact, the instability strip covers the same temperature range than in Fig.7, $T_{\text{bump}} \in [1.8, 2.3]$, but it becomes almost vertical as there is no critical value of σ to trigger off the destabilisation of the layer. In other words, there is a degeneracy in σ as this parameter is not affecting on the stability.

5.3.3. The $T_{\text{bump}} - e$ survey

Finally, we study the influence of the hollow width e on the stability by performing a survey in the (T_{bump}, e) -plane, while keeping constant \mathcal{A} and σ . Results are displayed in Fig. 9.

An instability strip of the same kind than the one shown in Fig. 7 is clearly visible as it exists a minimal value for the width e from which the fundamental mode becomes unstable ($e_{\text{min}} \simeq 0.15$). It means that narrow hollows are not sufficient to initiate the instability.

5.3.4. Summary of the surveys

These three parametric studies allow us to show the respective influence of the hollow parameters on the layer stability:

- In Figures 7-9, we found a particular range in T_{bump} , i.e. $T_{\text{bump}} \in [1.8, 2.3]$, within which the fundamental mode is unstable. It defines an instability strip in temperature

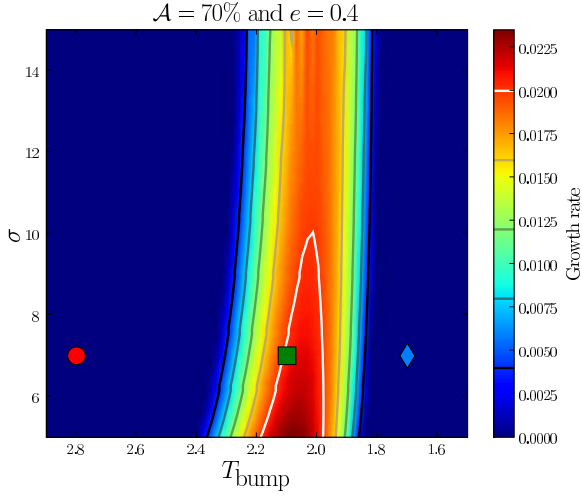


Fig. 8. Instability strip for the fundamental mode in the plane $(T_{\text{bump}}, \sigma)$, for given values of \mathcal{A} and e . The blue diamond, green square and red circle correspond to the same modes displayed in Fig. 7.

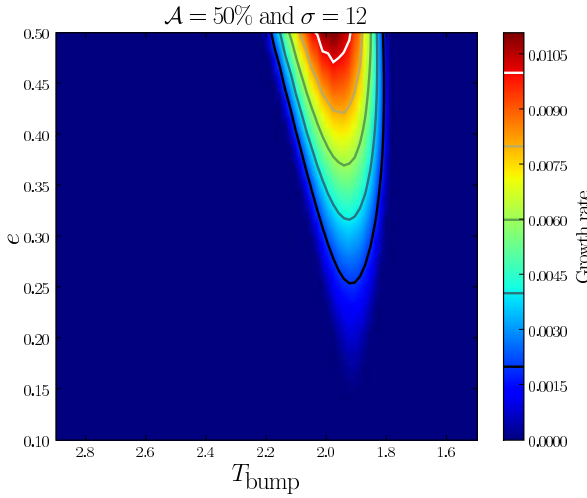


Fig. 9. Instability strip for the fundamental mode in the plane (T_{bump}, e) , for given values of \mathcal{A} and σ .

and corresponds to the particular area in the layer we introduced before as the transition region.

- Only the amplitude and width of the hollow have an influence on the stability as we found critical values for both of them, i.e. $\mathcal{A}_{\text{min}} \simeq 45\%$ and $e_{\text{min}} \simeq 0.15$. This can be linked to the condition (13) which entails that a precise shape in the conductivity profile is needed to get unstable modes. Moreover, the hollow slope σ is not a key control parameter as it does not modify the shape of the instability strip while varying.

We are now going to clarify these propitious conditions thanks to the work integral formalism.

5.4. Work integral in the non-adiabatic case

By generalising to the non-adiabatic case the demonstration done in Appendix A.1, we obtain the following expression for the exact (complex) eigenvalue

$$\lambda = \frac{\int_0^1 \left[\frac{\gamma - 1}{\gamma} T_0(\theta + R) \frac{du_z^*}{dz} - gRu_z^* + \mathcal{D}_\nu u_z^* \right] \rho_0 dz}{\int_0^1 |u_z|^2 \rho_0 dz}. \quad (41)$$

As the denominator is always positive, the sign of the real part τ only depends on the numerator one. To separate the regions of damping from the ones of driving, we thus plot the real part of the work integral in Fig. 10b.

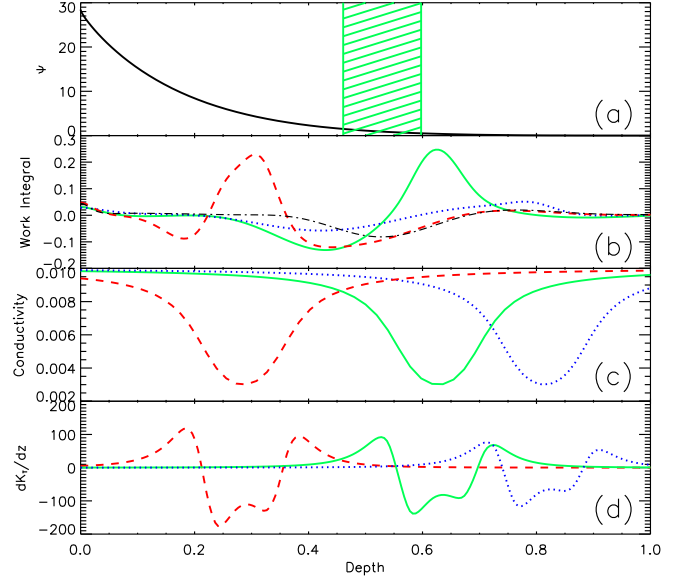


Fig. 10. **a)** Coefficient Ψ plotted over the entire box (Eq. 20). The green superimposed hatched zone represents the location where $\Psi = 1 \pm 0.5$. **b)** The real part of the work integral numerator (Eq. 41) plotted for the three different equilibrium models already discussed in Figs. 3 and 6. The case with a constant radiative conductivity is superimposed as a dot-dashed black line. **c)** Corresponding radiative conductivity profiles. **d)** Corresponding equilibrium field $d\mathcal{K}_T/dz$.

The work integral is really useful as it is possible to precisely check where the driving occurs. The criteria given in Eq. (22) predict that for a “sufficient” hollow, i.e. with a sufficient amplitude and width located in the transition region, the fundamental mode will be unstable. This result has already been checked thanks to the parametric study (Fig. 7 for example). With the work integral, we consider the same three particular modes studied before in Figs. 3 and 7:

- The first one, plotted in dotted blue, expresses a case of a hot star where ionisation region is next to the surface. In this case, ionisation region is located in a place where density is really small, and thus $\Psi \ll 1$. In Fig. 10b, we compare this case to the one with a constant radiative conductivity, for which $K_O(T_0) = K_{\text{max}}$ and $d\mathcal{K}_T/dz = 0$, and we can conclude that the conductivity hollow has a little influence on the work integral in this case: driving is unable to prevail over damping and $\tau < 0$.

- In the second case, plotted in solid green, the radiative conductivity begins to decrease significantly at the location of the transition region where $\Psi \simeq 1$. As a consequence, driving is important in this place (Eq. 22). In addition, the radiative conductivity increase occurs in a place where non-adiabatic effects are already significant, i.e. $\Psi < 1$. This means that no damping will occur between the hollow position and the surface because the radiative flux perturbations are “frozen in”. Driving is overcoming damping in this case and thus, $\tau > 0$.
- The third case, plotted in dashed red, denotes a cold star where ionisation region is located deeper in the stellar atmosphere where $\Psi \gg 1$. As shown in Fig. 6, ionisation occurs there in a quasi-adiabatic place. As a consequence, excitation provided by the conductivity hollow cannot balance the damping arising in the layer, thus $\tau < 0$.

In conclusion, Fig. 10 illustrates both conditions given in Eq. (22): (i) it is first necessary to have $d\mathcal{K}_T/dz < 0$ to drive the oscillations. But this condition is not sufficient to sustain the κ -mechanism; (ii) indeed, the thermal engine underlying the conductivity hollow has to be located neither too deep in the star, nor too close to the surface. Therefore, only a specific range of effective temperatures allows the overlap of the transition and ionisation regions, which leads to the instability strips found in Figs. 7-9.

6. Direct Numerical Simulations

In order to confirm all of the instability strips arising in the previous linear stability analysis, we performed direct numerical simulations of the *nonlinear* problem. That is, starting from the most favourable setups found during the parametric surveys, we advanced in time the nonlinear hydrodynamic equations to check:

- the onset of the instability sustained by the κ -mechanism and thus confirm the growth rates of the linear stability analysis.
- the nonlinear saturation of the instability, which is of course not caught in the linear analysis, and have an estimation of the final amplitudes of modes.

All DNS have been done using the Pencil Code⁵. This non-conservative code is a high-order centered finite difference code (of the sixth order in space and third order in time) and conserved quantities are kept up to the discretization error of the scheme. On multiprocessor computers, it uses the MPI libraries (Message Passing Interface) which allow communications between processors and thus runs in parallel. Moreover, this code is a fully explicit one as the computation of the solution at time t^{n+1} depends on the solution obtained at time t^n before. The timestep dt is therefore limited by an usual Courant-Friedrichs-Levy (CFL) condition based on the consideration of the smallest physical timestep existing in the simulation as

$$dt \leq \min \left(c_{\delta t} \frac{\delta x}{c_{s_{\max}}}, c_{\delta t \chi} \frac{\delta x^2}{\chi_{\max}}, c_{\delta t \nu} \frac{\delta x^2}{\nu_{\max}} \right), \quad (42)$$

where $c_{\delta t}$, $c_{\delta t \chi}$ and $c_{\delta t \nu}$ are constant coefficients depending on the spatial order of the scheme (see §19.2 in Press et al. 1992, hereafter PTVF92).

⁵ See <http://www.nordita.org/software/pencil-code/> and Brandenburg & Dobler (2002).

6.1. The needed of an implicit solver

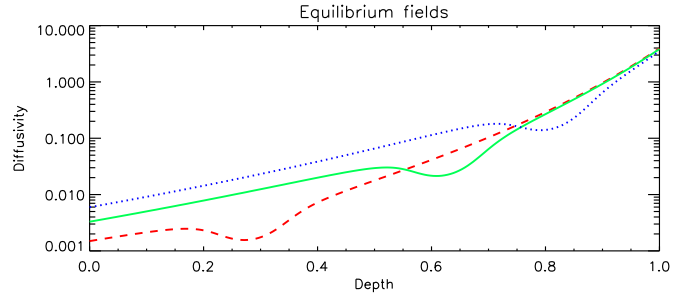


Fig. 11. Three different diffusivity profiles with $T_{\text{bump}} = 1.7$ (dotted blue line), $T_{\text{bump}} = 2.1$ (solid green line) and $T_{\text{bump}} = 2.8$ (dashed red line).

This CFL condition is clearly a problem in our case as the most favourable setups imply very large radiative diffusivities at the surface. Fig. 11 emphasises this point where the diffusivity profile is plotted for the three common hollows used in this work ($T_{\text{bump}} = [1.7, 2.1, 2.8]$). Because the Ψ -criterion (21) imposes a weak value of Δm and hence of the top density, one gets large surface values for the radiative diffusivity $\chi = K/\rho c_p \simeq 3$ in all cases. It means that the corresponding radiative diffusion timestep $c_{\delta t \chi} \delta x^2 / \chi_{\max}$ entering in Eq. (42) will be the smallest one and will impose a very small timestep dt . As an example, if we consider a typical spatial resolution of 256×256 (i.e. 256 gridpoints in each direction), we obtain $dt \sim 10^{-6}$ whereas the dynamics of the layer is rather constrained by the sound speed of which the dynamical timescale is $\delta x / c_{s_{\max}} \simeq 3 \times 10^{-3}$.

It is therefore numerically prohibitive to reach the nonlinear saturation of excited acoustic modes with such an explicit solver. To limit the number of iteration, we have decided to solve the diffusion of temperature *implicitly*. In fact, as implicit schemes are unconditionally stable, we have no more constraints on the timestep coming from radiative diffusion and thus the CFL becomes

$$dt \leq \min \left(c_{\delta t} \frac{\delta x}{c_{s_{\max}}}, c_{\delta t \nu} \frac{\delta x^2}{\nu_{\max}} \right), \quad (43)$$

giving $dt \sim 10^{-3}$ for the same resolution 256×256 .

6.2. The Alternate Direction Implicit (ADI) scheme

In order to solve the temperature equation, we adopt the time-split formulation given in Malagoli et al. (1995). We thus solve first explicitly the three hydrodynamic equations, i.e. density, velocity and temperature, but without solving the radiative diffusion term at this step. We then solve the temperature diffusion with the intermediate temperature $T_{\text{expl}}^{n+1/2}$ treated as a source term.

The time advance of the diffusion temperature equation is treated implicitly in the form

$$\frac{T^{n+1} - T^n}{dt} = \frac{T_{\text{expl}}^{n+1/2} - T_{\text{expl}}^n}{dt} + \mathcal{R}, \quad (44)$$

where the radiative diffusion term \mathcal{R} is expressed by

$$\begin{aligned} \mathcal{R} &= \frac{1}{2} \frac{1}{\rho_{\text{expl}}^{n+1/2} c_v} \text{div} [K(T^{n+1}) \nabla T^{n+1} + K(T^n) \nabla T^n] \\ &= \frac{1}{2} [\Lambda_x(T^{n+1}) + \Lambda_x(T^n) + \Lambda_z(T^{n+1}) + \Lambda_z(T^n)]. \end{aligned} \quad (45)$$

\mathcal{R} could be directly dealt with a Cranck-Nicholson method and a single matrix inversion with, for instance, a Successive Over Relaxation (SOR) method. For a 2-D problem, this approach forces us to invert a very sparse $N^2 \times N^2$ matrix (e.g. §19.5 in PTVF92). That is why we have decided to implement an Alternate Direction Implicit (ADI) scheme which relies on operator splitting theory which is frequently used in diffusion problems (e.g. §19.3 in PTVF92; Dendy 1977; Masalkar 1994). It allows us to deal with tridiagonal matrices (or cyclic ones depending on the boundary conditions used) by solving implicitly both directions successively.

To treat implicitly the nonlinear terms (i.e. $K(T)$) we have adopted the following approximation commonly called Rosenbrock's method (Saarikoski et al. 1997; Witelski & Bowen 2003)

$$\Lambda(T^{n+1}) = \Lambda(T^n) + \underbrace{\left(\frac{\partial \Lambda}{\partial T^n} \right)}_{\equiv J} (T^{n+1} - T^n), \quad (46)$$

where J denotes the Jacobian matrix associated with the operator Λ . Expanding Eq. (44) in each direction thus leads to

$$\begin{cases} \left(I - \frac{dt}{2} J_x \right) \alpha = \Lambda_x(T^n) + \Lambda_z(T^n) + \frac{T_{\text{expl}}^{n+1/2} - T_{\text{expl}}^n}{dt} \\ \left(I - \frac{dt}{2} J_z \right) \beta = \alpha \\ T^{n+1} = T^n + dt \cdot \beta, \end{cases} \quad (47)$$

where I , J_x and J_z are the identity matrix, a cyclic one and a tridiagonal one, respectively.

6.3. Results

All 2D-simulations were carried out using a mean resolution 16×201 and a constant kinematic viscosity $\nu = 5 \times 10^{-4}$. In order to avoid as much as possible the propagation of nonradial modes (Mulet-Marquis et al. 2007), we chose a ‘‘small’’ box with an aspect ratio $L_x/L_z = 1$. Indeed, if we refer to classical hydrodynamic instabilities, the critical horizontal wavelength λ_{crit} from which the instability develops is generally a bit larger than the vertical extent L_z of the domain. As an example, $\lambda_{\text{crit}}/L_z = 2\sqrt{2} = 2.83$ in the Rayleigh-Bénard convection (Chandrasekhar 1961) or $\lambda_{\text{crit}}/L_z = 2.84$ in the compressible polytrope $m = 1$ (Gough et al. 1976).

6.3.1. Growth rates from the DNS

Fig. 12 emphasises the temporal evolution of the mean momentum $\langle \rho u_z \rangle$ (where $\langle \cdot \rangle$ is an average over the entire box)

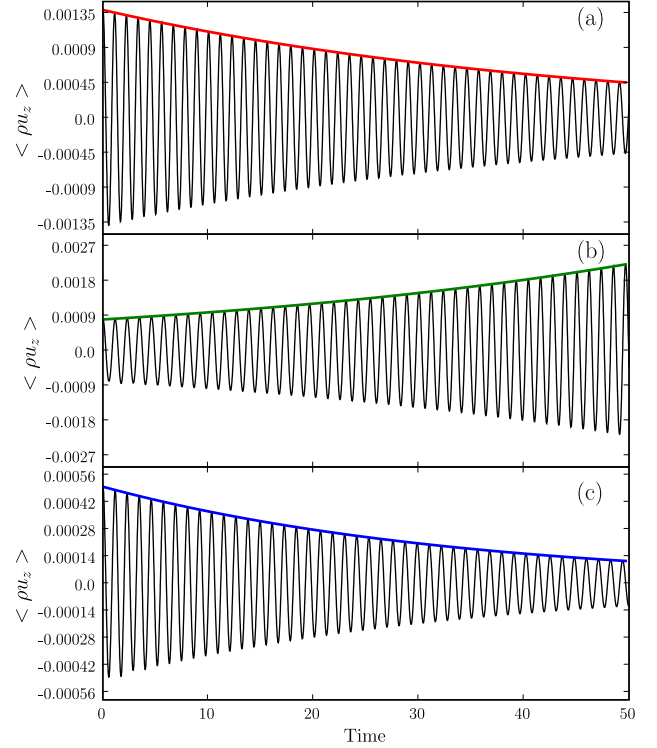


Fig. 12. The temporal evolution for times $t \in [0, 50]$ of the mean vertical momentum $\langle \rho u_z \rangle$ with the three different starting setups. In each panel, the growing (or damping) curve calculated thanks to the linear stability analysis is superimposed. **a)** $T_{\text{bump}} = 2.8$ (red line). **b)** $T_{\text{bump}} = 2.1$ (green line). **c)** $T_{\text{bump}} = 1.7$ (blue line).

Table 1. Growth rates corresponding to the three equilibrium setups given in Fig. 12 computed in the linear stability analysis (the real part of eigenvalues) and in the DNS (computed from the exponential growth of the vertical momentum). The corresponding relative error is also given.

	τ_{LSB}	τ_{DNS}	Rel. err.
red	-2.2415×10^{-2}	-2.2412×10^{-2}	1.5551×10^{-4}
green	2.0484×10^{-2}	2.0516×10^{-2}	1.5286×10^{-3}
blue	-2.9382×10^{-2}	-2.9339×10^{-2}	1.4877×10^{-3}

for the three common equilibrium setups (the red, green and blue ones corresponding to $T_{\text{bump}} = [2.8, 1.7, 2.1]$). Only one case appears to be unstable as:

- The first (red) setup expresses the case of a cold star where ionisation region is deep. The linear stability analysis achieved before predicts that no excitation will occur in this case (the red circle in Fig. 7 is well outside the instability strip). As seen in Fig. 12a, this result is confirmed by the nonlinear simulation as the mean vertical momentum decreases with time. Moreover, the damping rate calculated with LSB (superimposed as a

- red line) is reproduced with a great agreement in this simulation (Table 1).
- The second (green) setup denotes the case where the κ -mechanism is efficient. As a consequence, the fundamental p-mode is expected to be unstable (the green square inside the instability strip in Fig. 7). The DNS confirms this excitation (Fig. 12b) and the growth rate is the same as the predicted one (Table 1).
 - The third (blue) one corresponds to a hot star where ionisation is next to the surface. In this case, damping phenomena prevail over excitation and the fundamental mode is stable (the blue diamond outside the instability strip in Fig. 7). One more time, the result is confirmed by the DNS (see Fig. 12c and Table 1).

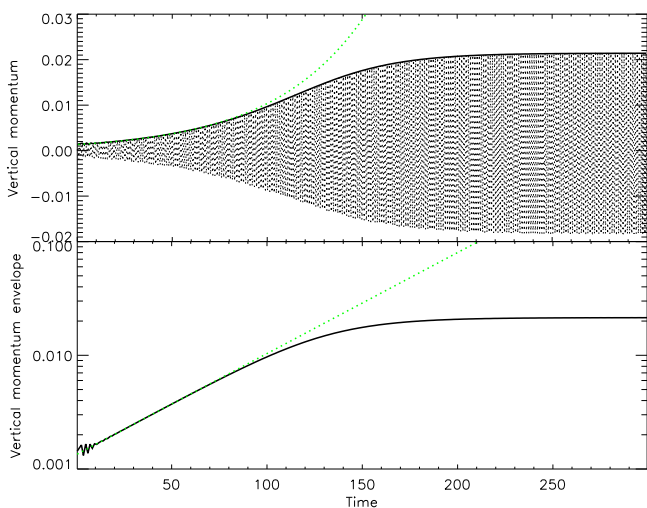


Fig. 13. *Upper panel:* temporal evolution of the mean vertical momentum $\langle \rho u_z \rangle$. The linear stability analysis result from Fig. 4 is superimposed in green. *Lower panel:* temporal evolution of the corresponding envelope with the theoretical curve of the growth still superimposed. Ordinate is scaled logarithmically.

In Fig. 13, we have integrated the DNS from the initial green setup with $T_{\text{bump}} = 2.1$ till the approach to the nonlinear limit cycle stability, that is, the nonlinear saturation. The (green) dotted line corresponds to the theoretical growth rate given in Table 1, that is, $\tau = 2.0484 \times 10^{-2}$. The saturation of this mode appears to be achieved around time $t \simeq 200$, which roughly corresponds to 170 mode periods. Such time interval is compatible with the characteristic timescale of the instability given by $1/\tau \sim 100$. Finally, the amplitude reached at the end of the saturation is about $\langle \rho u_z \rangle \simeq 2 \times 10^{-2}$. A careful study of the modes saturation is beyond the scope of this paper and will be developed in future works.

6.3.2. Vertical profiles

The good agreement between the theoretical and DNS growth rates shown in Table 1 marks a first success in reproducing the κ -mechanism in our simulations. We next address the point of the modes structure by computing the

vertical profiles from the DNS and comparing them to the eigenvectors of the linear stability analysis.

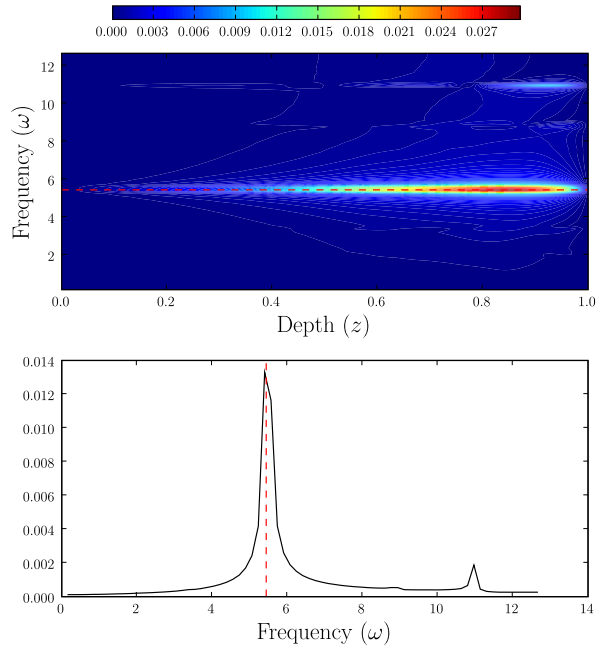


Fig. 14. *Upper panel:* temporal power spectrum in the (z, ω) -plane for the radial modes $k_x = 0$. *Lower panel:* the resulting spectrum after an integration in depth. Dotted lines correspond to the theoretical frequency $\omega_{00} \simeq 5.44$ obtained in the linear stability analysis (e.g. Fig. 4).

In Fig. 14, we have performed an horizontal and temporal Fourier transforms of the vertical velocity field and plotted the resulting power spectrum at $k_x = 0$ in the plane (z, ω) -plane. With this method, we are able to determine exactly which acoustic modes are excited or not in our numerical experiment as they emerge in this plane as “shark fin” peaks around given frequencies (see Dintrans & Brandenburg 2004). That is indeed what is displayed in Fig. 14 where the radial acoustic mode with a frequency $\omega_{00} \simeq 5.44$ is excited and the agreement with the linear eigenfrequency is remarkable. The second overtone with $\omega_{02} \simeq 11.05$ also appears in the (z, ω) -plane, with still a good agreement between the linear stability analysis and the DNS. In fact, one can note that this frequency is almost twice the fundamental mode one. It means that a resonance-like interaction occurs between these two modes: the κ -mechanism excites the fundamental mode and a nonlinear interaction transfers some energy between this mode and the second *damped* overtone, leading to the nonlinear saturation.

As we have computed, thanks to LSB, the eigenfunctions from a given equilibrium setup (see Fig. 4), one can compare them to the vertical velocity u_z deduced from the power spectra in Fig. 14. That is what is displayed in Fig. 15 where a mean profile around the frequency $\omega_{00} = 5.44$ has been computed. The DNS profile and the linear stability analysis one perfectly overlap meaning that we both have an agreement on the temporal (i.e. the frequency) and spatial (i.e. the pattern) scales of this mode.

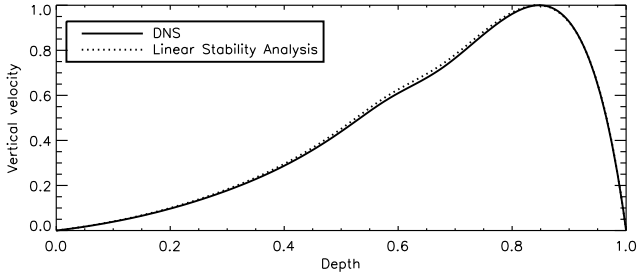


Fig. 15. Comparison between normalised vertical velocity profiles u_z deduced from the DNS power spectrum (solid line) and the linear stability analysis (dashed line).

7. Conclusion

We have modeled κ -mechanism in Cepheids by a similar physical problem: the propagation of radial acoustic waves in a partially ionised shell. Our model consists in a perfect gas embedded in an entirely radiative layer and the ionisation region has been depicted by a configurable hollow in radiative conductivity. This approach allows to quickly change the shape and location of this ionised region in the layer through the hollow parameters T_{bump} , \mathcal{A} , σ and e (Eqs. 25-26). We first have checked that a hollow with a sufficient amplitude and width may lead to

$$\frac{d\mathcal{K}_T}{dz} < 0, \quad (48)$$

which corresponds to the classical instability criterion derived from the work integral and quasi-adiabatic considerations. Nevertheless, another condition is needed to obtain a thermal heat engine in Eddington's sense: the ionisation region has to be located at a certain place in the layer, neither too deep nor too close to the surface. We have shown that this propitious area is located in the so-called *transition zone* separating the quasi-adiabatic interior from the strongly non-adiabatic surface. This thermodynamical criterion can be summarised by

$$T_{\text{ionisation}} \sim T_{\text{TR}} \quad \text{and} \quad \frac{\langle c_v T_{\text{TR}} \rangle \Delta m}{\Pi L} \sim 1. \quad (49)$$

With this second criterion, appropriate boundary conditions have been chosen in order to have a transition region in the middle of our box for the fundamental acoustic mode. Both radiative and hydrostatic equilibria have then been discretized on the (spectral) Gauss-Lobatto grid and solutions have been computed thanks to a linear solver. Once done, we have performed a linear stability analysis by computing the whole spectrum as well as associated eigenvalues for the radial oscillations equations.

The main advantage of our approach lies in its ability to make the parameters of the conductivity hollow vary. The major result of parametric surveys is the checking of the previous conditions by way of the appearing of instability strips: only configurations satisfying both conditions (48-49) have led to unstable fundamental modes (e.g. Figs. 7 and 10).

Then, these most favourable setups found in the linear stability analysis have been the starting points of our first 2-D (nonlinear) DNS of κ -mechanism. However, because of a too restrictive Courant-Friedrichs-Levy (CFL) condition

at the surface, these setups were not well-suited for a fully explicit code such as the Pencil Code one. We therefore have developed a new *implicit* module to deal with the radiative diffusion term and thus soften the CFL constraint. These DNS have confirmed with a great agreement both growth rates and structures of linearly unstable modes (see Figs. 13 and 15). Moreover, we have been able to reach the nonlinear saturation which involves an intricate coupling between the fundamental mode and (at least) the damped second overtone of which the period is a multiple of the fundamental one.

This work constitutes a first step in our Cepheids' project devoted to the modelling of the convection-pulsation interaction in the coldest Cepheids close to the red edge of the instability strip. Indeed, it is well known that convection occurs in a non-negligible part of these stars and modify the pulsation properties. For now, models based on time-dependent convection theories reproduce quite well the position of this red edge or, say, observational periods and light curves (YKB98; Bono et al. 1999). However, they involve many free parameters which are either fitted to the observations or hardly constrained by theoretical values, leading to almost similar results for different parameter sets (Kolláth et al. 2002; Szabó et al. 2007).

Despite their own limitations (their weak contrasts in pressure through the computational domain or their thermal timescale problem, see e.g. Brandenburg et al. (2000)), DNS are without a doubt a good way to address this convection-pulsation interaction as they fully take into account the crucial nonlinearities. With a conductivity profile solely based on temperature (Eq. 25), it is easy to *locally* shape one (or several) convective zone by increasing the temperature gradient above the adiabatic one. Indeed, as an ionisation region corresponds to a local increase in opacity, it is well known that convection can develop there. This occurs in cold Cepheids where two separate convectively unstable regions superimpose with the HeI/H and HeII ionisation regions. By adjusting in DNS the convective zone width or the strength of gravity, it will be possible to match the (local) turnover timescale of convection with the mean mode period, and then to study the coupling between convection and pulsation.

Acknowledgements. Calculations were carried out on the CalMip machine of the Centre Interuniversitaire de Calcul de Toulouse (CICT) which is gratefully acknowledged. It is also a pleasure to thank Isabelle Baraffe, Fabien Dubuffet, Marie-Jo Goupil and Michel Rieutord for their fruitful comments.

Appendix A: Work Integral

A.1. Using the quasi-adiabatic approximation

In the energy equation in Syst. (3), we can first separate adiabatic terms from non-adiabatic ones as

$$T' = T'_{\text{adia}} - \frac{1}{\rho_0 c_v \lambda} \text{div } \mathbf{F}', \quad (A.1)$$

and, by using the ideal gas equation of state (1),

$$p' = p'_{\text{adia}} - \frac{\gamma - 1}{\lambda} \text{div } \mathbf{F}'. \quad (A.2)$$

This equation corresponds to the pressure perturbation due to both adiabatic and non-adiabatic oscillations. The momentum equation in Syst. (3) then becomes

$$\begin{aligned}
(\lambda + \delta\lambda)(\mathbf{u} + \delta\mathbf{u}) = & \underbrace{-\frac{1}{\rho_0}\nabla p'_{\text{adia}} + \frac{\rho'_{\text{adia}}}{\rho_0}\mathbf{g}}_{\text{Adiabatic part}} \\
& + \underbrace{\frac{1}{\rho_0}\frac{\gamma-1}{\lambda}\nabla(\text{div}\mathbf{F}')}_{\text{Non-adiabatic perturbation}}. \quad (\text{A.3})
\end{aligned}$$

This equation can formally be written as a generalised eigenvalue problem with a perturbation operator

$$(A + \delta A)(\boldsymbol{\psi} + \delta\boldsymbol{\psi}) = (\lambda + \delta\lambda)B(\boldsymbol{\psi} + \delta\boldsymbol{\psi}), \quad (\text{A.4})$$

where $\delta\lambda$ and $\delta\boldsymbol{\psi}$ are caused by the perturbation operator δA (here the non-adiabatic effects). $\delta\lambda$ can then be obtained from a first-order perturbation analysis equivalent to these done in quantum mechanics (e.g. Bender & Orszag 1978; Dyson & Schutz 1979)

$$\delta\lambda = \frac{\langle \boldsymbol{\psi}_0 | \delta A \boldsymbol{\psi}_0 \rangle}{\langle \boldsymbol{\psi}_0 | B \boldsymbol{\psi}_0 \rangle}, \quad (\text{A.5})$$

where the symbol $\langle | \rangle$ means the following dot product (e.g. Lynden-Bell & Ostriker 1967)

$$\langle \mathbf{f}_1 | \mathbf{f}_2 \rangle = \int_V \mathbf{f}_1^* \cdot \mathbf{f}_2 \rho_0 dV. \quad (\text{A.6})$$

We thus obtain the expression for the eigenvalue perturbation $\delta\lambda$

$$\delta\lambda = \frac{\gamma-1}{\lambda} \frac{\int_V \mathbf{u}^* \cdot \nabla(\text{div}\mathbf{F}') dV}{\int_V |\mathbf{u}|^2 \rho_0 dV}. \quad (\text{A.7})$$

We can go a step further using

$$\mathbf{u}^* \cdot \nabla(\text{div}\mathbf{F}') = \text{div}(\mathbf{u}^* \text{div}\mathbf{F}') - \text{div}\mathbf{u}^* \text{div}\mathbf{F}', \quad (\text{A.8})$$

of which the first term in the RHS vanishes due to the rigid boundaries for the velocity as

$$\int_V \text{div}(\mathbf{u}^* \text{div}\mathbf{F}') dV = \oint_S \mathbf{u}^* \text{div}\mathbf{F}' \cdot d\mathbf{S} = 0. \quad (\text{A.9})$$

The second term in the RHS can also be simplified by using the continuity equation

$$\text{div}\mathbf{u}^* = -\lambda^* \frac{\delta\rho^*}{\rho_0}, \quad (\text{A.10})$$

where $\delta\rho$ is the Lagrangian perturbation of density. We finally get the expression for the eigenvalue perturbation in the non-adiabatic case as

$$\delta\lambda = -\frac{\int_V (\gamma-1) \frac{\delta\rho^*}{\rho} \text{div}\mathbf{F}' dV}{\int_V |\mathbf{u}|^2 \rho_0 dV}, \quad (\text{A.11})$$

where we have assumed that the adiabatic eigenmode is purely imaginary, that is $\lambda = i\omega$, and thus $\lambda^*/\lambda = -1$. We note that $\Re(\delta\lambda)$ corresponds to the damping (or growing) rate of a non-adiabatic mode, commonly written τ .

A.2. A thermodynamical approach

It is also possible to derive Eq. (A.11) by energetic considerations. Hereafter, we will essentially follow Hansen's demonstration (Hansen & Kawaler 1994). Let us adopt a thin shell of mass dm at a certain radius. During a complete cycle of oscillations the work dW done by the shell on its surroundings is linked to the internal energy dU and heat dq gained by this shell through the first principle of thermodynamics

$$dq = dU + dW. \quad (\text{A.12})$$

Integrating over a cycle of oscillations leads to

$$\oint dq = \oint dU + \oint dW. \quad (\text{A.13})$$

We are now going to suppose that the oscillation mechanism is quasi-adiabatic. It implies that every thin shell dm behaves as a Carnot-like heat engine where each process is reversible and the shell comes back to its initial position after each cycle of oscillations. Internal energy dU being a state variable, one gets $\oint dU = 0$ hence

$$W = \oint dq. \quad (\text{A.14})$$

Now one applies the second principle of thermodynamics claiming that

$$dS = \frac{dq}{T}. \quad (\text{A.15})$$

After some time elapsed, we have $T = T_0 + \delta T$ and then

$$dS = \frac{dq}{T_0} - \frac{\delta T}{T_0^2} dq, \quad (\text{A.16})$$

as a first-order approximation, with $\oint dS = 0$ for the same reason than U . We thus write

$$\oint dq = \oint \frac{\delta T}{T_0} dq. \quad (\text{A.17})$$

With Eqs. (A.14) and (A.17), the work over a cycle is given by

$$W = \oint \frac{\delta T}{T_0} dq, \quad (\text{A.18})$$

which leads to the total work integrated over mass shells

$$W_{\text{tot}} = \int_M \oint \frac{\delta T}{T_0} dq dm. \quad (\text{A.19})$$

If $W_{\text{tot}} > 0$, the star produces work over a cycle of oscillations and the initial perturbation will grow. In this case, the star is driving pulsation which is thus unstable. It may occur when shells gain heat (i.e. $dq > 0$) during compression phases (i.e. $\delta T > 0$) and this is the so-called ‘‘valve-mechanism’’ proposed by Eddington (1917).

Let us write the energy equation in the form

$$dq = -\frac{1}{\rho_0} \text{div}\mathbf{F}' dt, \quad (\text{A.20})$$

and substitute it in Eq. (A.19)

$$\frac{dW_{\text{tot}}}{dt} = - \int_V \frac{\delta T}{T_0} \text{div } \mathbf{F}' dV. \quad (\text{A.21})$$

Kinetic energy over a period of oscillations is given by

$$E = \frac{1}{2} \int_V |\mathbf{u}|^2 \rho_0 dV, \quad (\text{A.22})$$

and Eqs. (A.21-A.22) lead to the following expression for the growth rate of a mode

$$\tau = \frac{1}{2} \frac{dW_{\text{tot}}/dt}{E}. \quad (\text{A.23})$$

Note that the factor 1/2 comes from the fact that the pulsation amplitude grows or decays one half as does energy. The two formulations Eqs. (A.11) and (A.23) are of course alike by assuming the quasi-adiabatic approximation $\delta T/T_0 \simeq (\gamma - 1)\delta\rho/\rho_0$.

Appendix B: The radiative term in energy equation

Radiative flux perturbations can be written as

$$- \text{div } \mathbf{F}' = \text{div} (K_0 \nabla T' + K' \nabla T_0). \quad (\text{B.1})$$

By assuming $\theta \equiv T'/T_0$ and using Eq. (6), it entails

$$- \frac{d}{dz} \mathbf{F}' = \text{div} \left(K_0 T_0 \frac{d\theta}{dz} + K_0 \theta \frac{dT_0}{dz} + K_0 \mathcal{K}_T \theta \frac{dT_0}{dz} \right) \mathbf{e}_z. \quad (\text{B.2})$$

We then expand \mathcal{K}_T with equilibrium equations (29) as

$$\mathcal{K}_T = \frac{d \ln K_0}{d \ln T_0} = - \frac{T_0}{F_{\text{bot}}} \frac{dK_0}{dz}, \quad (\text{B.3})$$

and thus obtain

$$- \text{div } \mathbf{F}' = \frac{d}{dz} \left(K_0 T_0 \frac{d\theta}{dz} + K_0 \theta \frac{dT_0}{dz} + \theta T_0 \frac{dK_0}{dz} \right). \quad (\text{B.4})$$

Finally, one gets

$$- \text{div } \mathbf{F}' = \frac{d^2}{dz^2} (K_0 T_0 \theta) = \Delta_z (K_0 T_0 \theta). \quad (\text{B.5})$$

References

- Arnoldi, W. E. 1951, QApMa, 9, 17
 Baker, N. & Kippenhahn, R. 1962, Zeitschrift für Astrophysik, 54, 114
 Baker, N. & Kippenhahn, R. 1965, ApJ, 142, 868
 Bender, C. M. & Orszag, S. A. 1978, Advanced Mathematical Methods for Scientists and Engineers (Advanced Mathematical Methods for Scientists and Engineers, New York: McGraw-Hill, 1978)
 Böhm-Vitense, E. 1958, Zeitschrift für Astrophysik, 46, 108
 Bono, G., Marconi, M., & Stellingwerf, R. F. 1999, ApJS, 122, 167
 Brandenburg, A. & Dobler, W. 2002, CoPhC, 147, 471, [arXiv:physics/0111569]
 Brandenburg, A., Nordlund, A., & Stein, R. F. 2000, Geophysical & Astrophysical Convection, ed. P. A. Fox & R. M. Kerr (New York: Gordon and Breach Science Publishers)
 Buchler, J. R. 1997, in Variables Stars and the Astrophysical Returns of the Microlensing Surveys, ed. R. Ferlet, J.-P. Maillard, & B. Raban, 181
 Carson, T. R. 1976, ARA&A, 14, 95
 Chandrasekhar, S. 1961, Hydrodynamic and hydromagnetic stability (International Series of Monographs on Physics, Oxford: Clarendon, 1961)
 Christensen-Dalsgaard, J. 2003, Lecture Notes on Stellar Oscillations (Physical and Astronomical Institute of Aarhus University)
 Cox, J. P. 1958, ApJ, 127, 194
 Cox, J. P. 1963, ApJ, 138, 487
 Cox, J. P. 1980, Theory of stellar pulsation (Research supported by the National Science Foundation Princeton, NJ, Princeton University Press, 1980. 393 p.)
 Dendy, J. E. 1977, SJNA., 14, 313
 Dintrans, B. & Brandenburg, A. 2004, A&A, 421, 775, [arXiv:astro-ph/0311094]
 Dyson, J. & Schutz, B. F. 1979, Royal Society of London Proceedings Series A, 368, 389
 Eddington, A. S. 1917, The Observatory, 40, 290
 Fukushima, T. 1997, AJ, 113, 1909
 Gautschy, A. & Saio, H. 1996, ARA&A, 34, 551
 Gehmeyr, M. & Winkler, K.-H. A. 1992, A&A, 253, 101
 Gilliland, R. L., Bono, G., Edmonds, P. D., et al. 1998, ApJ, 507, 818
 Gough, D. O. 1977, ApJ, 214, 196
 Gough, D. O., Moore, D. R., Spiegel, E. A., & Weiss, N. O. 1976, ApJ, 206, 536
 Hairer, E., Norsett, S. P., & Wanner, G. 1993, Solving Ordinary Differential Equations I: Nonstiff Problems (Springer-Verlag: Berlin Heidelberg New York)
 Hansen, C. J. & Kawaler, S. D. 1994, Stellar Interiors. Physical Principles, Structure, and Evolution. (Stellar Interiors. Physical Principles, Structure, and Evolution, XIII, 445 pp. 84 figs. 3 1/2" diskette. Springer-Verlag Berlin Heidelberg New York. Also Astronomy and Astrophysics Library)
 King, D. S. & Cox, J. P. 1968, PASP, 80, 365
 Kolláth, Z., Buchler, J. R., Szabó, R., & Csubry, Z. 2002, A&A, 385, 932, [arXiv:astro-ph/0110076]
 Kuhfuß, R. 1986, A&A, 160, 116
 Lynden-Bell, D. & Ostriker, J. P. 1967, MNRAS, 136, 293
 Malagoli, A., Dubey, A., Cattaneo, F., & Levine, D. 1995, A Portable and Efficient Parallel Code for Astrophysical Fluid Dynamics, [http://astro.uchicago.edu/Computing/On-Line/cfd95/camelse.html]
 Masalkar, P. J. 1994, Optik, 4, 168
 Mihalas, D. & Weibel Mihalas, B. 1984, Foundations of radiation hydrodynamics (New York: Oxford University Press, 1984)
 Moler, C. B. & Stewart, G. W. 1973, SJNA., 10, 241
 Mulet-Marquis, C., Glatzel, W., Baraffe, I., & Winisdoerffer, C. 2007, A&A, 465, 937, [arXiv:astro-ph/0701371]
 Press, W. H., Teukolsky, S. A., Vetterling, W. T., & Flannery, B. P. 1992, Numerical recipes in FORTRAN. The art of scientific computing (Cambridge: University Press, 1992, 2nd ed.), **PTVF92**
 Saad, Y. 1992, Numerical Methods for Large Eigenvalue Problems (New York: Halsted Press)
 Saarikoski, H., Salmio, R. P., Saarinen, J., Eirola, T., & Tervonen, A. 1997, OptCo, 134, 362
 Seaton, M. J. & Badnell, N. R. 2004, MNRAS, 354, 457, [arXiv:astro-ph/0404437]
 Stellingwerf, R. F. 1982, ApJ, 262, 330
 Szabó, R., Buchler, J. R., & Bartee, J. 2007, ApJ, 667, 1150, [arXiv:astro-ph/0703568]
 Unno, W. 1967, PASJ, 19, 140
 Unno, W., Osaki, Y., Ando, H., Saio, H., & Shibahashi, H. 1989, Nonradial oscillations of stars (Nonradial oscillations of stars, Tokyo: University of Tokyo Press, 1989, 2nd ed.)
 Valdetarro, L., Rieutord, M., Braconnier, T., & Fraysse, V. 2007, JCoAM, 205, 382, [arXiv:physics/0604219]
 Vitense, E. 1953, Zeitschrift für Astrophysik, 32, 135
 Witelski, T. P. & Bowen, M. 2003, ApNM., 45, 331
 Wuchterl, G. & Feuchtinger, M. U. 1998, A&A, 340, 419
 Yecko, P. & Kollath, Z. 1998, in Astronomical Society of the Pacific Conference Series, Vol. 135, A Half Century of Stellar Pulsation Interpretation, ed. P. A. Bradley & J. A. Guzik, 94
 Yecko, P. A., Kolláth, Z., & Buchler, J. R. 1998, A&A, 336, 553, [arXiv:astro-ph/9804124], **YKB98**
 Zhevakin, S. A. 1953, Russ. A. J., 30, 161
 Zhevakin, S. A. 1963, ARA&A, 1, 367